Thin Solid Films 768 (2023) 139686

Contents lists available at ScienceDirect

Thin Solid Films

journal homepage: www.elsevier.com/locate/tsf

Energy-dependent dielectric tensor axes in monoclinic α-3,4,9,10-perylene tetracarboxylic dianhydride

M.I. Alonso [a,*], M. Garriga [a], J.O. Ossó [a,1], F. Schreiber [b], R. Scholz [c]

[a] Institut de Ciència de Materials de Barcelona, ICMAB-CSIC, Campus de la UAB, 08193 Bellaterra, Spain
[b] Institut für Angewandte Physik, Universität Tübingen, Auf der Morgenstelle 10, 72076 Tübingen, Germany
[c] Leibniz Institut für Polymerforschung, Hohe Straße 6, 01069 Dresden, Germany

ARTICLE INFO

Keywords:
Monoclinic dielectric tensor
Perylene tetracarboxylic dianhydride
Chromatic dispersion of tensor axes
Generalized ellipsometry
Electronic structure of organic semiconductor

ABSTRACT

We have determined the complex dielectric tensor of single crystalline 3,4,9,10-perylene tetracarboxylic dianhydride (α-PTCDA) as a function of energy in the range between 1.4 and 5.0 eV. The results obtained reflect the monoclinic symmetry of the crystal: The principal axes of the real and the imaginary part of the tensor in general do not coincide and show chromatic dispersion. Monoclinic behavior allows rotation of the components ε_X and ε_Z in the plane perpendicular to the unique symmetry axis Y. The experimental results indicate that the energies of the optical transitions observed in the weak ε_X component coincide with energies in which a resonance effect due to coupling with the stronger ε_Z component occurs. These resonances appear at energies close to electronic excitations such as the optical gap, the transport gap and the highest occupied molecular orbital–lowest unoccupied molecular orbital (HOMO–LUMO) peak-to-peak gap and their assignments are discussed based on theoretical calculations.

1. Introduction

Spectroscopic ellipsometry (SE) is a very powerful technique to investigate both optical and structural properties of materials. In particular, it allows to determine the dielectric function over a wide spectral range, providing essential experimental information about the electronic properties of the materials and their optical behavior, that is, propagation and attenuation of light traveling in the material. A characteristic trait of SE is that the parameters of interest are not always directly obtained from the measured spectra. Often, it is necessary to analyze the measured data by least-squares fitting procedures using calculated data for a model that represents the sample [1]. The only case where the ellipsometric measurements give the dielectric function in a rather straightforward way is the case of a bulk sample with perfect surfaces [2]. If we focus on crystalline samples, the simplest case is that of a cubic crystal, hence optically isotropic, where one measurement suffices to determine its complex dielectric function. However, as the crystal symmetry decreases, an increasing number of spectra must be measured and combined to determine all dielectric tensor components [3,4]. In optically uniaxial crystals of tetragonal or hexagonal symmetries at least two measurements are required, whereas in biaxial crystals with orthorhombic symmetry, at least three spectra are needed [2,5]. In all these cases the dielectric axes (principal axes of the dielectric tensor) are established by symmetry and coincide with the crystallographic axes. Therefore, approximative methods [6–8] can deliver close estimates of the tensor components, although numerical procedures must generally be used to extract accurate optical spectra from the measurements. In this context, biaxial crystals with monoclinic or triclinic symmetries are more complex. The latter is the most general case in which none of the dielectric axes is fixed by the crystal symmetry. Some studied cases are pentacene [9] and $K_2Cr_2O_7$ [10]. Despite this complication, in such a general case, the dielectric tensor can be solved by fitting the exact numerical solution of the ellipsometric equations [5] to the measured data. Even if it is not indispensable, symmetries detected in Mueller matrix measurements can be helpful to locate the axes [11], in a similar way as established methods using polarized microscopy [3,12]. In any case, data cross correlations are frequent, and therefore a larger number of spectra than required are usually measured in order to find a reliable solution by overdetermining the unknowns.

In this work, we have applied the general formalism described elsewhere [5] to obtain the dielectric function of a monoclinic crystal, namely the α polymorph of 3,4,9,10-perylene tetracarboxylic dianhydride (α-PTCDA) [13]. The space group of α-PTCDA is $P2_1/c$ with a monoclinic angle $\beta_c = 98.8°$ and lattice parameters $a = 0.374$ nm,

* Corresponding author.
E-mail address: isabel.alonso@icmab.es (M.I. Alonso).
[1] Present address: HEMPEL A/S, 08213 Polinyà, Barcelona.

https://doi.org/10.1016/j.tsf.2023.139686
Received 24 August 2022; Received in revised form 20 December 2022; Accepted 8 January 2023
Available online 13 January 2023

b = 1.196 nm, and c = 1.734 nm [14] with two symmetry equivalent molecules per unit cell. The planar molecules have a rectangular geometry defining a long and a short molecular axis along their major and minor axis, respectively. The two basis molecules lie almost flat (±5°) on the crystal {102} planes forming a herringbone, and the {102} planes are cleavage faces. Although we have investigated a single crystal, this compound has been studied as a paradigm in organic molecular beam deposition (OMBD) [15,16] as it tends to grow rather robustly, in most cases with the (102) planes nearly parallel to the substrate [17–19] forming high-quality thin films apt for device applications. Because of the short (102) interplanar distance of 0.32 nm [14,20] between π-stacked molecules, PTCDA also retains significant attention as an archetypical organic semiconductor (OSC). In many of these OSC systems, the optical properties are a key to the understanding of their functional and device performance [21–23].

In the context of the present study, we particularly focus on the anisotropy of the optical properties of PTCDA in the visible and near ultraviolet range of optical absorption. Some of the anisotropic optical properties of single crystalline α-PTCDA were previously studied in this spectral region [24]: From ellipsometric measurements with different orientations of the plane of incidence in highly symmetric positions [6] relevant in the sample, six distinct spectra of $\langle n \rangle$ and $\langle k \rangle$ were obtained, identifying the energies and polarizations of the main electronic excitations present in the visible range (between 1.5 and 3.7 eV). This procedure allowed to separate differently polarized excitonic excitations in the (102) molecular planes and approximately perpendicular to them. However, one of the key features of monoclinic crystals is rotation of the principal dielectric axes within the ac plane as a function of the frequency, which was later on demonstrated in PTCDA [5] at several energies. For the particular case of PTCDA, with the molecular transition dipoles lying in the (102) plane and the stacking of molecules perpendicular to this plane, it is reasonable to expect that optical excitations in the crystal remain (102) in-plane or out-of-plane polarized. However, some optical transitions deviate from this expectation causing the observed axes rotation. Dielectric axes rotation effects have been reported in some inorganic monoclinic crystals in the infrared range mainly connected to lattice vibrations [25,26] and in the optical range of absorbing crystals both in inorganic β−Ga_2O_3 [27], and in organic crystals such as α-PTCDA and anthracene [5]. The effect has also been demonstrated in the transparency range of inorganic crystals [27–29].

Here we report on the full dielectric tensor of α-PTCDA in the spectral range accessible to our setup, from 1.4 to 5 eV. Eight independent spectra (i.e., four complex tensor components) are needed to fully describe the monoclinic dielectric tensor. At each measured energy, we have determined the set of principal dielectric axes X, Y, and Z, as defined in Fig. 1 and Section 4, and we have used them as the reference frame for the tensor representation which means that the eight spectra describing the complete tensor $\overleftrightarrow{\varepsilon}$ will correspond to the six components of the two diagonalized second-rank tensors ε_1 and ε_2, and to the two Euler angles α_1 and α_2 that describe their respective orientations in a given reference frame of laboratory axes x, y, and z (see Section 4). The results show that, in general, the angles α_1 and α_2 do not coincide, and therefore the real ε_1 and imaginary ε_2 dielectric function ellipsoids are non-collinear. This situation is particularly clear around three energies where a resonant effect due to interaction between components occurs, and pronounced rotation of the axes is evident. These resonances seem to be connected to critical points of the joint density-of-states of the highest occupied molecular orbital (HOMO) band and the lowest unoccupied molecular orbital (LUMO) band, the energies being near the optical gap, the transport gap, and the HOMO-LUMO peak-to-peak gap of the material. These possible assignments will be critically discussed in Section 6.

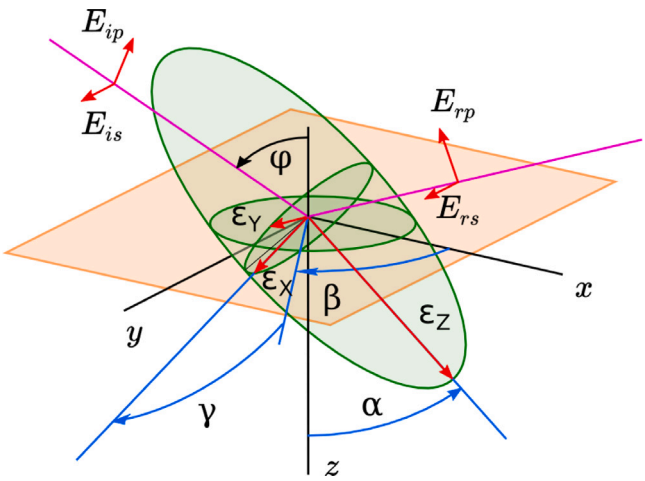

Fig. 1. Graphical representation of one component (real or imaginary) of the biaxial dielectric tensor as an ellipsoid with three principal components ε_X, ε_Y, and ε_Z along its principal axes X, Y, and Z. The sketch represents a measurement configuration of a general crystal surface under an angle of incidence φ. The Jones vector components of the incident and reflected light beams are (E_{ip}, E_{is}) and (E_{rp}, E_{rs}), respectively. The Eulerian angles (α, β, γ) give the orientation of the principal axes with respect to the laboratory axes x, y, and z.

2. Optical excitations of PTCDA in the visible and near UV

Below its ionization potential, a PTCDA molecule has several dipole-allowed electronic excitations with oscillator strength above 0.01, having their transition dipoles exclusively along the long or short molecular axis [30]. Hence, none of these transitions provides a sizable oscillator strength along the molecular normal.

The visible range is dominated by a strong electronic excitation which can easily be determined from solution spectra, or estimated from time-dependent density functional theory (TD-DFT). In solvents with particularly weak interactions like superfluid helium, the HOMO-LUMO excitation shows a fundamental transition at E_{00} = 2.602 eV [31]. Together with an electronic reorganization energy around 0.15 eV deduced from the vibronic progression of PTCDA dissolved in dimethyl sulfoxide (DMSO) [32,33] and a reorganization energy of about 0.015 eV arising from low-frequency breathing modes [34], this places the vertical electronic transition of a free molecule in the frozen ground state geometry at about 2.77 eV. The solvent DMSO exerts a red shift as large as about 0.24 eV with respect to superfluid helium (or vacuum), as calculated from the absolute E_{00} with respect to all modes: 2.602 eV (superfluid helium) and 2.365 eV (in DMSO). In crystalline PTCDA, the red shift of the HOMO-LUMO transition becomes even larger. The second lowest electronic transition of PTCDA occurs around 3.3 eV in poly-crystalline films [32,35]. With TD-DFT calculations, these observed transition energies are reproduced reasonably well, assigning a quite large oscillator strength to the HOMO-LUMO transition, and a second lowest dipole-allowed transition which is about 10 times weaker [30]. Moreover, from these TD-DFT calculations, several dipole-allowed electronic excitations with transition dipole within the molecular plane are expected in the range from 4 to 6 eV, with a cumulative oscillator strength exceeding that of the HOMO-LUMO band by far. They contribute to a known quite strong absorption band around 5.5 eV [36,37]. Hence, in the near UV covered by the ellipsometry data presented below, these higher transitions will contribute significantly above 4.5 eV, whereas the visible range is dominated by the HOMO-LUMO transition, and the second lowest dipole-allowed electronic transition provides two well-resolved vibronic subbands around 3.3 and 3.45 eV.

Besides these intramolecular excitations, the crystalline phase allows for various intermolecular charge transfer (CT) excitations [38].

As discussed previously [30], with respect to the difference between ultraviolet photoelectron spectroscopy (UPS) of the HOMO band and inverse photoelectron spectroscopy (IPES) of the LUMO band involving charge excitations of molecules close to the sample surface, the lowest optically excited CT state is strongly red-shifted: the UPS-IPES peak-to-peak gap occurs around 4.0 eV [39] or 3.78 eV [40]. The strong red shift of optically excited CT states results from a larger polarization shift within the bulk crystal with respect to surface molecules, and from Coulomb attraction between the electron and the hole state. Hence, as all optically excited CT states involve molecules in direct contact, in particular stack neighbors, the very large Coulomb attraction of electron and hole places this kind of excitation far below a CT energy defined from a difference between energies found in photoemission or inverse photoemission. Close to the crystal surface, due to a reduced polarization shift, optically excited CT states would experience a small blue shift with respect to the bulk. However, as the oscillator strength of CT states is about 2 orders of magnitude smaller than for neutral molecular excitations, a modified CT energy close to the surface can only have a marginal influence onto the dielectric function. For very thin films of only a few PTCDA monolayers, it was demonstrated that the optical response differs from the bulk [41] also due to changes in packing geometry [42]. Calculations along the stacking direction reveal that already for slabs of a few molecular layers, the optical response rapidly converges to the bulk crystal [43,44]. As differences with respect to the bulk rely on a modified optical response of the topmost monolayer with a thickness of 0.32 nm only, its impact on our comparison with ellipsometry data can be ignored. Obviously, the electron–hole attraction depends on the geometric arrangement of the two charged molecules involved, placing CT along the stacking direction at the lowest energy [38], but several other geometries are likely to provide higher lying HOMO-LUMO CT states within a range accessible to our ellipsometry setup.

For PTCDA and other perylene compounds, a comprehensive exciton model involving neutral molecular excitations and CT between stack neighbors has been developed, allowing to calculate the interference between both types of optical excitations [45]. This model can assign the difference between the lowest CT energy and the neutral molecular excitation energy (abbreviated with F, indicating Frenkel exciton) quite precisely, arriving at estimates of $E_{00}^{\mathrm{F}} = 2.17$ eV and $E_{00}^{\mathrm{CT}} = 1.93 \pm 0.07$ eV, the latter value corroborated by subsequent photoluminescence excitation (PLE) measurements, placing the fundamental CT transition along the stack at $E_{00}^{\mathrm{CT}} = 1.95$ eV [46]. Up to now, PTCDA is the only known compound where $E_{00}^{\mathrm{CT}} < E_{00}^{\mathrm{F}}$ in the crystalline phase, as corroborated by various types of spectroscopic probes, involving in particular PLE [46] and photoluminescence [47,48]. It is important to note that this exciton model does not cover CT states of different geometry. At energies above the range of the strong intramolecular HOMO-LUMO transition, the ellipsometry data presented below will give evidence for weak optical transitions along the molecular normal (or more precisely orthogonal to a specific (102) plane in the crystal, as explained below in more detail). These contributions to the linear optical response cannot be assigned to the lowest CT transition below the intramolecular HOMO-LUMO transition, but instead, they are likely to correspond to higher lying CT states [38].

3. Experimental

The measurements presented in this study were performed on a single crystal of α-PTCDA obtained by temperature step sublimation under vacuum [49]. The needle-like shaped crystal had very good quality as-grown facets, and the ellipsometric measurements were performed at room temperature as quickly as possible after growth to minimize their degradation which in this material happens rather slowly. A SOPRA ES4G rotating polarizer spectral ellipsometer with a 75 W high-pressure Xe arc lamp and a double prism/grating monochromator of 750 mm equivalent focal length with a multialkali photomultiplier tube was used to measure in the range from 1.4 to 5 eV with a resolution of about 1 meV. The software codes used for calibration of the ellipsometer and data acquisition were written in house to improve correction of both systematic and random errors in the data. In particular, statistical errors were determined by averaging several measurements of every data point, and these error bars were taken into account in subsequent fitting procedures. The crystal was mounted like in a single-crystal X-ray diffractometer, glued on the tip of a thin glass fiber that could be attached to a sample holder allowing sufficient tilt of the sample to position the facet to be measured normal to the plane of incidence. The tip mount was necessary because the collimated light beam (spot size ca. 1×3 mm^2 at the angle of incidence) was larger than the measured facets (between 0.1 to 0.5 mm wide). In this way only the light reflected from the crystal face of interest was collected. An alignment telescope allowed to orient the plane of incidence relative to the crystal position with a precision of $\pm 1°$. The sample holder was equipped with a goniometer that allowed azimuthal sample rotations perpendicular to the surface normal, and at least 16 azimuths in the range from 0 to 360 degrees were measured for each energy. The angle of incidence was fixed at $\varphi = 65°$, and spectra were recorded as a function of energy with a step of 0.02 eV and up to four analyzer angles $A = 5, 10, 20, 30°$. For the initial measurements we selected two facets, one on the side of the needle and the other on the needle tip to collect enough spectra at very different crystal orientations in order to obtain sensitivity to all tensor components. Later, we cleaved the crystal and measured the fresh cleavage face. The consistency of these spectra with those of the as-grown facets indicates the cleanliness of the measured surfaces, so that we consider that no corrections for overlayers are needed [7]. A sketch of the crystal after cleaving is drawn in Fig. 2(a). The measured facets were identified and labeled after the ellipsometry measurements following standard procedures of optical mineralogy and crystallography [12] using the habit of the crystal, X-ray diffraction, and optical observation in polarized light. X-ray diffraction confirmed that the crystal was α phase, but not all faces could be indexed. Optically, the larger (ca. 0.5×1 mm^2) side facet measured was identified as a (001) plane because in crossed polarizers it showed sharp symmetric extinction in white light, and the angle formed with the cleavage plane measured by observation under the microscope was approximately 120 degrees (not crystallographically consistent with (100), the only other possible orientation). The angle between the cleavage plane $(\bar{1}0\bar{2})$ and (001) is 120.6 degrees from X-ray structure data [14,20]. Therefore, as a convenient reference for the laboratory axes, the monoclinic b axis was identified as the crystal edge at the intersection between $(\bar{1}0\bar{2})$ and (001) planes. These assignments were seen to be consistent with the ellipsometric measurements. The facet on the needle tip could not easily be identified using crossed polarizers since no particular optical symmetry was evident. By direct examination under the microscope, it was observed to form an angle of approximately 50 degrees with the (001) plane – and therefore approximately 70 degrees with the $(\bar{1}0\bar{2})$ plane – with a slight inclination of about 10 degrees for the b axis off that plane. Independently, from analysis of many detailed ellipsometry azimuthal scans (including azimuths every 5 degrees), we found 52 ± 2 degrees and 14 ± 3 degrees for these inclinations. The method to find these values was explained in detail in Ref. [5]. In addition, the azimuthal angle indicating when the b axis was on the plane of incidence determined from ellipsometry or directly observed from the crystal morphology coincided within 2 degrees. Using crystallographic data, it follows that the only orientation that matches the mentioned angles is the $(1\bar{1}\bar{3})$ plane. The relevant crystallographic facets are depicted in Fig. 2 as well as the position of the molecules relative to each one of these orientations.

4. The monoclinic dielectric tensor

In general, a dielectric tensor $\overleftrightarrow{\varepsilon}$ at a given energy is completely described by 12 magnitudes corresponding to the two (real and imaginary) diagonal second-rank tensors and their respective orientations

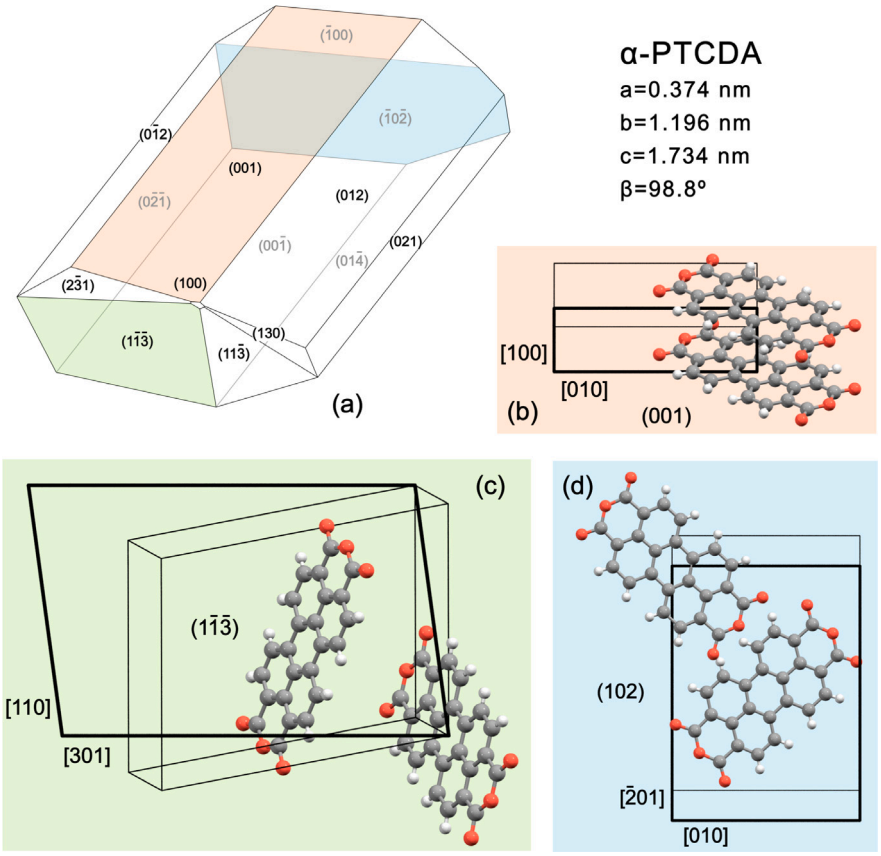

Fig. 2. (a) Drawing of the actual crystal morphology indicating the measured facets and their crystallographic orientations. (b) Projection of the unit cell perpendicular to the measured (001) plane and the relative position of two stacked molecules. (c) Projection onto the $(1\bar{1}\bar{3})$ plane, indicating the two basis molecules in the unit cell. (d) Projection perpendicular to the (102) cleavage plane showing the projection of the two basis molecules lying almost flat onto this plane. The reference axes defining the crystal orientation in our experiment were chosen related to this plane (yz plane) where $y \parallel [010]$ is the monoclinic axis b, $z \parallel [\bar{2}01]$, and the x axis is perpendicular to this plane.

given by Euler angles in a reference orthogonal coordinate system x, y and z. The graphical representation of $\overleftrightarrow{\varepsilon}$ is an ellipsoid as a consequence of the "Principal axis theorem" that establishes a bijective correspondence between symmetric matrices and quadratic forms [50]. The notation used here is $\overleftrightarrow{\varepsilon}_j = (\varepsilon_{j1}, \varepsilon_{j2})$, where $j = X, Y, Z$ denote the principal tensor axes, and the numeric subindices $m = 1$ and 2 mean real and imaginary, respectively. We denote the Euler angles as β_m, α_m, and γ_m using the "zxz" convention used by Berreman [51] with the correspondences $\alpha \to \theta$, $\beta \to \phi$, and $\gamma \to \psi$. Note that $(\varepsilon_X, \varepsilon_Y, \varepsilon_Z, \alpha, \beta, \gamma)$ and $(\varepsilon_X, \varepsilon_Y, \varepsilon_Z, \pi - \alpha, \pi + \beta, \pi - \gamma)$ represent exactly the same dielectric tensor. Thus α can be restricted to the range $[0, \pi/2]$. Note also that in an experiment a variation of the angle β means an azimuthal rotation of the sample about its normal, and the origin value $\beta = 0$ defines together with α and γ the sample surface orientation with respect to the tensor axes. In other words, the laboratory axes defined by the measured surface and the plane of incidence as defined in Fig. 1 are different for every different measured surface. For monoclinic symmetry, the crystallographic monoclinic axis b must be a principal axis of $\overleftrightarrow{\varepsilon}$, reducing the number of unknowns to 8: The six ε_{jm} components and two α_m that give the tilt of the real and imaginary ellipsoids. Taking this into account, in this work, to relate the three measured surfaces we choose as common reference the laboratory axes referred to the (102) plane. In the used convention, α gives the inclination of the Z axis, so that for $\alpha = 90°$ the Z axis is on the (102) plane. When $\gamma = 0°$ the X axis is in that plane, and if $\gamma = 90°$ the Y axis is in that plane. In addition, when $\beta = 0, 180°$ the plane of incidence contains the Y axis.

The dielectric tensor in the chosen reference axes x, y and z is:

$$\overleftrightarrow{\varepsilon} = \begin{pmatrix} \varepsilon_{xx} & 0 & \varepsilon_{xz} \\ 0 & \varepsilon_{yy} & 0 \\ \varepsilon_{zx} & 0 & \varepsilon_{zz} \end{pmatrix}, \tag{1}$$

where y coincides with the unique symmetry axis b, and $\varepsilon_{xz} = \varepsilon_{zx}$. Because b is a symmetry axis, it is also a principal dielectric axis, and the corresponding component ε_{yy} is a principal value of the tensor. However, the lack of further symmetry axes allows intermixing between the other components ε_{xx} and ε_{zz} in the crystallographic plane ac perpendicular to the unique axis b. This intermixing is given by the nondiagonal components ε_{xz}, whose magnitude will depend on the specific choice of the laboratory axes x and z in the ac plane, as also the values ε_{xx} and ε_{zz} depend on this choice.

We can also write the tensor in diagonal form at each energy:

$$\overleftrightarrow{\varepsilon} = \begin{pmatrix} \varepsilon_X & 0 & 0 \\ 0 & \varepsilon_Y & 0 \\ 0 & 0 & \varepsilon_Z \end{pmatrix}. \tag{2}$$

This has the advantage of being a physically and optically intuitive representation in terms of principal components with well defined values which are represented as the lengths of the ellipsoid axes X, Y, and Z, as drawn in Fig. 1. The ellipsoid corresponds to the graphical representation of a symmetrical second-rank tensor where, in this case, the existence of the non-diagonal contribution is translated into a rotation of the X and Z axes in the plane perpendicular to Y (b axis). Since the principal X and Z axes are in general different for the real and the imaginary part, when needed we use subindices 1,2 to denote real and imaginary magnitudes, respectively. Each set of principal axes can be related to the frame of orthonormal reference axes x, y, and z using Euler angles, as described above and elsewhere [51,52]. The tilt angles α_1 and α_2 describing the interaction between X and Z components reflect the actual rotation of the dielectric ellipsoids ε_1 for the real part and ε_2 for the imaginary part of the dielectric response about the symmetry axis Y. Of course, the orientations of the

components $\varepsilon_{yy1} = \varepsilon_{Y1}$ and $\varepsilon_{yy2} = \varepsilon_{Y2}$ along the b axis of the crystal remain invariant. The other tensor components given in Eq. (1) can be calculated from those of Eq. (2), where the components of the real part of the dielectric tensor are mixed according to the rotation angle $\Delta\alpha_1$,

$$\begin{aligned}\varepsilon_{xx1} &= \varepsilon_{X1}\cos^2(\Delta\alpha_1) + \varepsilon_{Z1}\sin^2(\Delta\alpha_1)\\ \varepsilon_{zz1} &= \varepsilon_{X1}\sin^2(\Delta\alpha_1) + \varepsilon_{Z1}\cos^2(\Delta\alpha_1)\\ \varepsilon_{xz1} &= \varepsilon_{zx1} = (\varepsilon_{Z1} - \varepsilon_{X1})\sin(\Delta\alpha_1)\cos(\Delta\alpha_1),\end{aligned} \tag{3}$$

and similarly for the imaginary component of the dielectric tensor involving the angle α_2. In Eq. (3) the rotation angle $\Delta\alpha_1 = \alpha_1 - \alpha_{plane}$ is referred to an actual plane of the crystal containing the monoclinic axis. This surface could be chosen such that $\alpha_{plane} = 0$, however, our choice for PTCDA preserves the usual optical convention where ε_{xx1} in the transparency range has the lowest value, placing the laboratory x axis perpendicular to a {102} crystal plane. In terms of the defined Euler angles, $\alpha_{(102)} = 90°$. Conversely, the rotation angles and the principal components calculated from the non-diagonal ones are given by:

$$\begin{aligned}\tan 2(\Delta\alpha_1) &= 2\varepsilon_{xz1}/(\varepsilon_{zz1} - \varepsilon_{xx1})\\ \varepsilon_{X1} &= \varepsilon_{xx1} - \varepsilon_{xz1}\tan(\Delta\alpha_1)\\ \varepsilon_{Z1} &= \varepsilon_{zz1} + \varepsilon_{xz1}\tan(\Delta\alpha_1).\end{aligned} \tag{4}$$

5. Results of the ellipsometric analysis

In this study, the ellipsometric equations are solved using the principal components of Eq. (2) as parameters. The details to solve the ellipsometric equations are explicitly explained in Ref. [5], the solution method is based on the 4 × 4 generalized matrix algebra [53,54] on an energy-by-energy basis. The method is totally general and no specific crystal orientations or *a priori* knowledge of the crystallographic information is needed, although this knowledge has to be incorporated for the analysis. For that, the laboratory axes must be predetermined with respect to the crystal lattice, allowing to deduce the measured orientation angles α_1 and α_2 of the principal axes of the dielectric tensor with respect to the crystal. The only fixed axis is the $y \equiv Y$ axis which must coincide with the $b \parallel [010]$ monoclinic axis. In the case of PTCDA, from the orientation of the HOMO-LUMO transition dipoles along the long axes of the two basis molecules, it is obvious that the largest dielectric response both in terms of refractive indices and of absorption is expected in the {102} planes, see Section 2. Therefore, by convenience, the yz plane in the laboratory axes is defined to be the $(\bar{1}0\bar{2})$ crystal plane, so the z axis is perpendicular to [010] and the x axis is then parallel to the $[\bar{2}01]$ direction. All relevant crystallographic axes and surfaces are indicated in Fig. 2.

Details of the fitting procedure and results at some energies were reported elsewhere [52]. The spectral fits presented in this work included data collected from $(1\bar{1}\bar{3})$, $(\bar{1}0\bar{2})$, and (001) planes. To relate data from the different crystal planes, each spectra contained the specific orientation of the laboratory axes given from the Euler angles: $\alpha_{(\bar{1}0\bar{2})} = 90°$, $\gamma_{(\bar{1}0\bar{2})} = 90°$, $\alpha_{(001)} = 30.6°$, $\gamma_{(001)} = 90°$, $\alpha_{(1\bar{1}\bar{3})} = 83.2°$, and $\gamma_{(1\bar{1}\bar{3})} = 76°$. The fit results provide the three principal elements of each dielectric tensor component ε_1 and ε_2 and their orientation with respect to the crystal as a function of energy in the range between 1.4 and 5 eV. Various spectra showing quite different spectral behaviors due to the different crystal orientations in the two most anisotropic crystal faces measured are plotted in Fig. 3 together with values calculated from the point-by-point fits. The values of $\cos\Delta$ obtained in the transparent region of the present measurement are mainly affected by depolarization caused by light reflected from the backside of the small crystal, most clearly in the (001) face due to the thin (ca. 0.1 mm) slab geometry. In this situation, below 2 eV, $\cos\Delta$ values are meaningless, but $\tan\Psi$ is almost unaffected [55], allowing to determine the real part. Some depolarization could still be present in the absorption spectral range due to roughness, which in the high-quality crystal grown facets is mainly associated with monomolecular steps and terraces, with a stacking molecular distance of 0.32 nm, similar to the surface layer described in Section 2. The associated inaccuracy in the maximum values of dielectric functions (both real and imaginary components) would be negligible for such low roughness. For about 10 monolayers standard roughness correction, we estimate an inaccuracy of about 5%, which we consider reasonable as maximum inaccuracy of the absolute values of the dielectric tensor components presented in the following. Fig. 4 displays the principal component fit result along the invariant symmetry axis. The other two components are plotted in Fig. 5. In Fig. 5(a) we plot the values of the angles $\Delta\alpha_1$ and $\Delta\alpha_2$ which give the inclination of the principal Z_1 and Z_2 axes from the $(\bar{1}0\bar{2})$ plane together with their uncertainties as determined from the fits. In general, the errors in the components are much smaller than the errors in the angles, which are drawn in Fig. 5(a). The results indicate that the principal axes of the real and the imaginary part in general do not coincide and show some chromatic dispersion. However, at most energies, the axes remain relatively close to the $(\bar{1}0\bar{2})$ crystal plane (within ~ ±10 degrees), coinciding with the expected larger values along the molecular transition dipoles, with the superposition of the transition dipoles of both basis molecules giving basically the ε_Z component. The two corresponding components are plotted together in Fig. 5(b). In this way we can see very clearly that energies where the angles show more spectral dispersion coincide with transitions present in the ε_X component. Besides, at the energies where the Z_j axes depart from the $(\bar{1}0\bar{2})$ plane, the values of ε_{Xj} and ε_{Zj} coincide.

Using Eqs. (3) we can calculate the differences due to the measured inclinations $\Delta\alpha_j$, if we would consider the tensor as fixed to the chosen reference axes. In this approximation, the ε_{Zj} components would be on the $(\bar{1}0\bar{2})$ plane and the ε_{Xj} components would be normal to it. The corrections are rather small for the *in-plane* component, i.e., $\varepsilon_{zz,j} \simeq \varepsilon_{Zj}$, and even for the *out of plane* component they are not very important, $\varepsilon_{xx,j} \simeq \varepsilon_{Xj}$. This means that for many practical purposes we can neglect these corrections in PTCDA as the values of non-diagonal components with our specific choice of x and z axes are rather small. Nevertheless, the variations of the angles α_j have other consequences that will be discussed below.

6. Optical behavior and monoclinic symmetry

We have seen that the corrections to the values of the optical constants introduced by the monoclinic rotation of the principal dielectric axes within the *ac* plane in PTCDA remain relatively small. The largest rotation effects are seen in the real part, where we observe two large dispersive features of the angle α_1 close to the energies 2.46 eV and 2.90 eV (see Fig. 5). At these energies the values of the two components interfering in the *ac* crystallographic plane become equal, that is, $\varepsilon_{X1} = \varepsilon_{Z1}$, giving rise to a singularity which is also apparent in Eq. (3). Since in the analysis of the experimental data, the values ε_{X1}, ε_{Z1}, and α_1 are obtained as independent parameters from the fitting procedure, one of the energies where we observe the crossing between the two real parts X and Z is slightly different, 2.46 eV and 2.95 eV (the experimental noise is also larger at the higher energy). Nevertheless the effect is clear, and from the point of view of the refraction properties, these singularities are a signature of the material becoming *uniaxial* when α_1 tends to ±45 degrees with the *real* optic axis coinciding with the monoclinic unique axis b. Note that in this limit the non-diagonal terms vanish, i.e., the real dielectric tensor is diagonal and the angle α_1 becomes meaningless because the real tensor becomes uniaxial. Between these two energies (2.46 eV and 2.95 eV) $\varepsilon_{X1} > \varepsilon_{Z1}$. The graphical representation of the solution at various measured energies is depicted in Fig. 6. Note that at the crossing points the material is not *truly* uniaxial because this exact coincidence only happens for the real parts. For the imaginary parts there is such a point around 3.9 eV where $\varepsilon_{X2} \simeq \varepsilon_{Z2}$, and a concomitant structure appears evidently in the angle α_2, despite the larger experimental errors in this spectral region due to much lower available light intensity. Near these singular points both

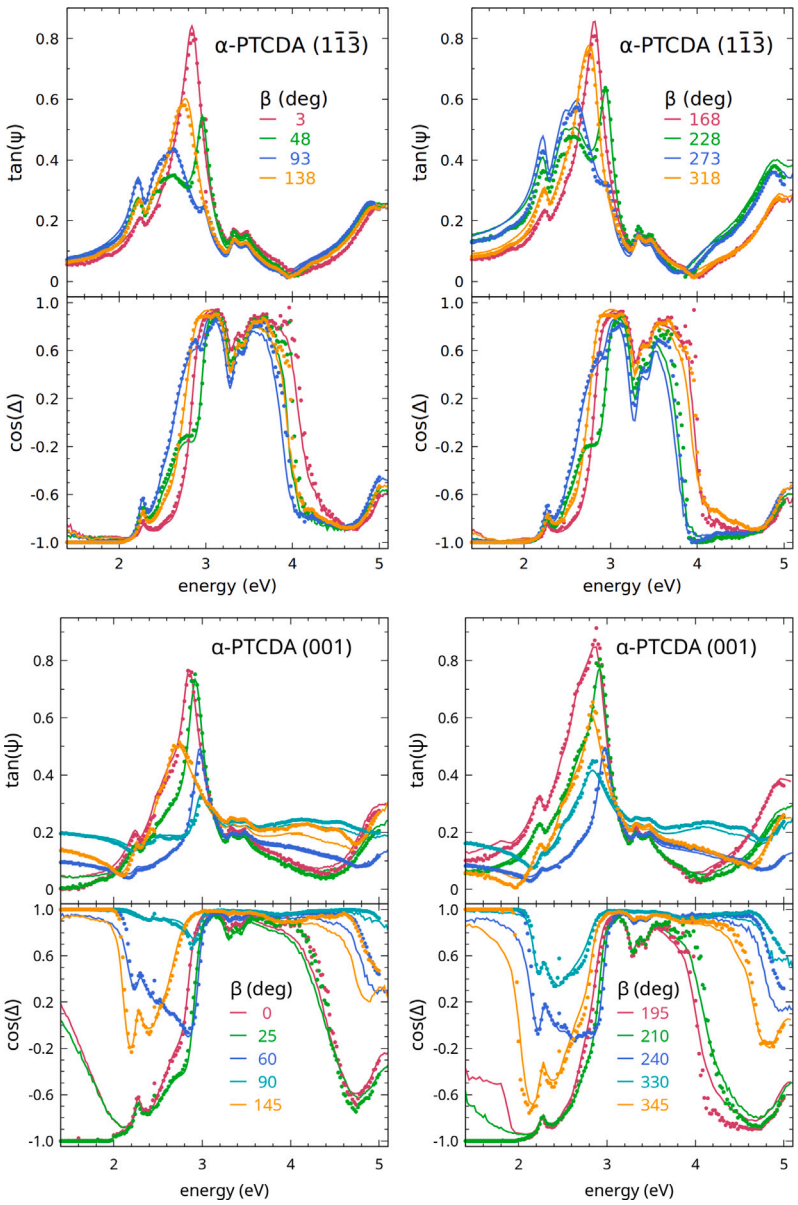

Fig. 3. Representative spectra measured at incidence $\varphi = 65°$ and analyzer angle 30° to illustrate quite different spectral behaviors as a function of the azimuthal angle β and orientation of the crystal surface. Measurements are drawn as lines and calculated values from the energy-by-energy fits are plotted as points. The plots are drawn in separate panels only for clarity.

of the real and the imaginary parts, the interaction between the mainly *out of plane* component ε_X and the mainly *in plane* component ε_Z is enhanced, resulting in an increased oscillator strength of the weaker component ε_X. Although the presence of structure in ε_X is intuitively associated to charge transfer (CT) excitons, the energies observed in this experiment are all above the lowest CT excitations calculated along the lattice vector a [45,46,56].

From self-consistent calculations of the polarization energies in molecular crystals, it is known that the CT energies are strongly red-shifted with respect to the difference between ionization potential and electron affinity in vacuum [38]. Moreover, when applying this formalism to PTCDA, it was found that the anisotropically screened Coulomb interaction between two oppositely charged molecular sites produces several low-lying CT states, the one for two molecules stacked along the lattice vector **a** being the lowest [38]. From a comprehensive exciton model including the Frenkel exciton manifold and this specific CT state, it was possible to constrain its vertical transition energy rather precisely to a value of 2.12 ± 0.07 eV, corresponding to an E_{00} transition energy of 1.95 ± 0.07 eV [45], in good agreement with an earlier estimate for the vertical transition energy of 2.14 ± 0.08 eV deduced from photoluminescence bands arising from CT states [30,47,48]. Together with the energy spacing between different CT states obtained from micro-electrostatic calculations [38], this allows to place the vertical transition energy of a further CT state along the lattice vector $(\mathbf{b}-\mathbf{c})/2$ at about 2.61 eV, and a CT state along $\mathbf{a}-\mathbf{b}/2+\mathbf{c}/2$ at 2.72 eV. The respective E_{00} transitions would be 0.17 eV lower, corresponding to 2.44 eV and 2.55 eV. Both values compare quite well to the lowest prominent contribution observed in the measured ε_{Xj} component of the dielectric tensor, so that we tentatively assign this spectroscopic feature either to CT along the lattice direction $(\mathbf{b}-\mathbf{c})/2$ or to CT along $\mathbf{a}-\mathbf{b}/2+\mathbf{c}/2$. The observed structure between 2.8 and 3.0 eV cannot be assigned to any CT state where the geometric contact between the molecules involved is still likely to produce a substantial oscillator strength, so that its interpretation remains rather unclear.

Together with the observed spectroscopic data in Fig. 5, we report the results of an exciton model including Frenkel excitons and CT states

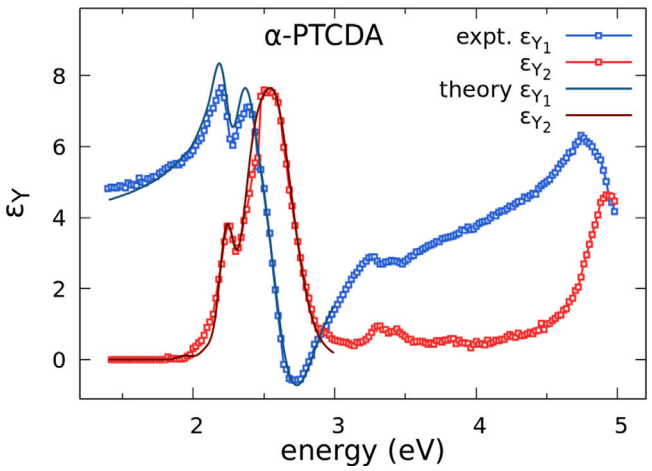

Fig. 4. Diagonalized ε_Y components obtained by point-by-point fitting compared to calculations relying on an exciton model involving neutral molecular excitations and CT states along stack neighbors. Y represents the monoclinic b axis, the only one fixed by symmetry.

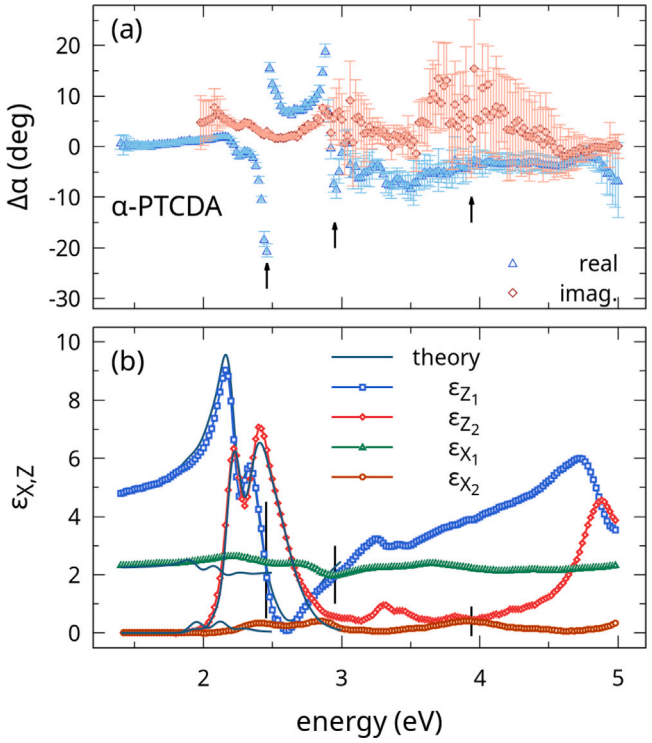

Fig. 5. Different components of the diagonalized dielectric tensor of α-PTCDA obtained by point-by-point fitting. (a) Angles of inclination of the principal axes for both real and imaginary ellipsoids in the chosen reference axes. When $\Delta\alpha_m = 0$, the corresponding Z_m axis is on the $(\bar{1}0\bar{2})$ plane and the X_m axis is perpendicular to this plane. Energies where clear deviations from $\Delta\alpha_m = 0$ are observed are marked by arrows. (b) Diagonalized ε_X and ε_Z components compared to the theoretical calculations. The energies where these components take the same value are marked by vertical lines. They coincide with the dispersive features observed in (a).

along the stacking vector **a** [45], applied later to PLE spectra [46]. The CT state with its fundamental transition $E_{00}^{\mathrm{CT}} = 1.95$ eV and the Frenkel exciton with $E_{00}^{\mathrm{F}} = 2.17$ eV interfere, producing two weak structures in the calculated tensor element ε_X around 1.95 eV and 2.10 eV, as currently reported in Fig. 5(b). Moreover, the mixing of Frenkel and CT contributions significantly modifies the lineshape of the two strong components of the dielectric tensor, ε_Y and ε_Z. The transition dipoles of Frenkel and CT states included in this model have been derived from time-dependent density functional theory using the hybrid functional B3LYP in a triple-ζ variational basis set, giving a CT transition with an oscillator strength of 1.8% of the neutral molecular excitation [45]. Based on these parameters, the calculated absorption of the CT states normal to the molecular planes remains quite weak, but the resulting values for ε_{X2} exceed the experimentally determined tensor element in this energy region, so that it is quite likely that the TD-DFT estimate is somewhat exaggerating the relative strength of the lowest CT transition. However, the calculated area below ε_{X2} over the range 1.9 to 2.3 eV is of similar magnitude as the measured features around 2.4 eV and 2.8 eV, so that the calculated size of the transition dipole and oscillator strength of the lowest CT state along the stacking direction **a** seems to be representative for the strength of the feature around 2.4 eV assigned tentatively to CT along the lattice direction $(\mathbf{b} - \mathbf{c})/2$ or along $\mathbf{a} - \mathbf{b}/2 + \mathbf{c}/2$. The band around 2.8 eV might correspond to some higher lying CT states, but due to the large number of possible candidates [38], a specific assignment cannot be provided.

The above comprehensive analysis of our ellipsometry data has allowed us to assign several optical transitions either to the interference between the lowest intramolecular excitation with CT along the lattice vector **a** (dominating the strong components ε_{Y2} and ε_{Z2} over the range 2 to 3 eV), to higher lying CT states (ε_{X2} around 2.4 and 2.8 eV), to the second lowest intramolecular excitation (peaks around 3.3 and 3.45 eV in strong components ε_{Y2} and ε_{Z2}), and to higher lying intramolecular transitions (above 4.5 eV in strong components ε_{Y2} and ε_{Z2}).

Previous investigations of PTCDA and other model compounds have made several attempts to relate intramolecular optical excitations to the energies of the valence band (DOS of HOMO states) and of the conduction band (DOS of LUMO states), to the definition of the so-called transport gap, and to optical CT excitations in the crystalline phase. With respect to peak energies derived easily from optical probes, UPS of the HOMO DOS, and IPES of the LUMO DOS, the transport gap involves a shift from the observed peaks towards midgap.

The traditional construction of the transport gap assumes a Gaussian DOS both for valence and conduction states. Concerning UPS, it is parameterized as $\mathrm{DOS}_{\mathrm{HOMO}} \propto \exp[-(E - E_{\mathrm{HOMO}})^2/(2\sigma_{\mathrm{HOMO}}^2)]$, places a tangent at the inflection point $E_{\mathrm{HOMO}} + \sigma_{\mathrm{HOMO}}$, and declares the footpoint of this tangent at $E_{\mathrm{HOMO}} + 2\sigma_{\mathrm{HOMO}}$ to correspond to the transport level of holes in the valence band. A similar construction applied to IPES data results in a transport level of $E_{\mathrm{LUMO}} - 2\sigma_{\mathrm{LUMO}}$ for electrons in the conduction band. Hence, with respect to the well-defined peak-to-peak gap $E_{\mathrm{LUMO}} - E_{\mathrm{HOMO}}$, the transport gap is lower by $2\sigma_{\mathrm{HOMO}} + 2\sigma_{\mathrm{LUMO}}$.

This construction has several caveats. First, the resolution of the respective experimental setup may contribute significantly to the observed broadening, so that the observed values of σ_{HOMO} and σ_{LUMO} may exceed the true broadening of the respective band. Second, the rigid shift into the gap does not account for a necessary dependence of the Fermi energy on the density of the respective charge carriers in valence band, conduction band, or both.

This second point is clarified most easily when analyzing photovoltaic devices based on bulk heterojunctions. At open circuit conditions, optical excitation and radiative or non-radiative recombination produce a thermodynamic equilibrium with a finite density of electrons and holes. Detailed investigations of the open circuit voltage as a function of temperature at constant illumination intensity have demonstrated that the open circuit voltage grows linearly when lowering the temperature, and that the interpolated limit towards zero temperature corresponds to the lowest radiative CT state at the donor–acceptor interface [57,58]. Moreover, there is clear evidence for a dependence of the open circuit voltage on illumination intensity [58,59], as expected from the thermodynamics of a photodiode [60], giving direct evidence that the Fermi energy (or transport level) within each band depends on the density of charge carriers.

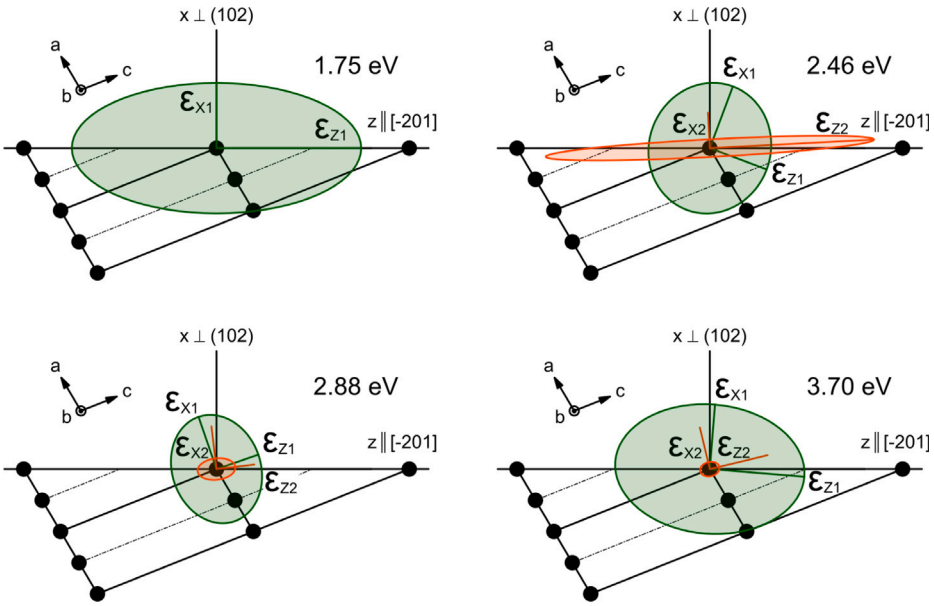

Fig. 6. Graphical representation of the obtained dielectric tensor projected onto the XZ plane at different measured energies, showing the X and Z components and their respective orientations, evidencing the chromatic dispersion of the dielectric axes. The components along the invariant Y axis (perpendicular to the paper) are not shown. The crystallographic axes and the indication of crystal unit cells are also displayed for reference. Note that the crystal fills all the space and the represented surfaces are only meant to provide a reference for the orientation of the tensors.

Even under these conditions, the construction of the transport gap for different blends may reproduce the observed trend of the open circuit voltage of the respective photovoltaic devices [61], but still the tangent construction for the definition of the transport gap has no advantage with respect to an analysis of the observed peaks of the respective DOS.

Of course, as charge carriers occupy only a tiny fraction of the available DOS of valence and conduction band, it is certainly true that the Fermi energy (or transport level) within each band is shifted towards midgap, and that the transport gap based on the tangent construction shows a better correspondence to the lowest optically accessible CT state than the difference between HOMO and LUMO peaks. However, the reason that this CT state occurs at lower energy results from the attractive Coulomb interaction at the shortest possible distance of the two molecules involved, and from a larger polarization shift in the bulk of a crystalline material with respect to molecules close to the surface involved both in UPS and IPES probes. For other studies of CT in alike molecules and its tuning, see Refs. [62,63]. Concerning PTCDA, these energies have been carefully calculated with microelectrostatic models [38], and their relation to IPES vs. UPS gaps [39] and different optical probes of CT states has been discussed before [30]. For donor–acceptor blends, DFT-based embedding schemes allowing to estimate the Coulomb binding energy of CT states at the donor–acceptor interface have become available, supporting the interpretation of spectroscopic signatures of CT states in a meaningful way [64,65].

The density of HOMO and LUMO electronic states in π-conjugated OSCs has been investigated using photoelectron spectroscopies [39,66]. The shape of the HOMO-LUMO joint density-of-states (DOS) in PTCDA allows to infer different energies which are very relevant, especially the transport gap which is determined by the DOS of the HOMO and LUMO band distributions. Although the interpretation of the relationship between the shape of these bands to electrical transport measurements may be slightly different, both Hill et al. [39] and Zahn et al. [66] obtained similar results. In both works the investigated samples were OMBD thin films of about 10 nm thickness evaporated from highly purified organic material in ultra-high vacuum environments. The energies quoted by Hill et al. [39] involved a bulk transport gap of 3.2(±0.4) eV and a HOMO-LUMO peak-to-peak gap of 4.0(±0.2) eV. Zahn et al. [66] located the transport gap at 2.74(±0.2) eV as the distance between the edges of the HOMO and LUMO band distributions and also measured 4.05(±0.2) eV as the peak-to-peak HOMO-LUMO distance. The most recent and probably most precise measurement of the peak-to-peak HOMO-LUMO energy amounts to 3.78 eV [40], giving a transport gap of 2.48 eV.

With respect to the HOMO-LUMO peak-to-peak distance, the excitonic optical gap is located at lower energies. According to Hill et al. [39] the optical gap of PTCDA is 2.6 eV whereas Zahn et al. [66] give a value of 2.22 eV. The difference between these two values is due to the concept of optical gap used by these authors, in the first case the energy of 2.6 eV is the energy of the absorption maximum of the sample, in the second case 2.22 eV is the lowest exciton peak. In our spectra these energies are clearly identified: The lowest exciton is a Davydov split doublet at 2.210 (Z)–2.247 (Y) eV, and the maximum absorption of 4.7×10^5 cm^{-2} is found at 2.62 eV in the ε_Y component.

In the monoclinic tensor, the first resonance observed occurs at 2.46 eV within the spectral region of transitions into the S_1 state manifold, and it corresponds to a cigar-shaped real part of the dielectric tensor with cylindrical symmetry, $\varepsilon_{Y1} > \varepsilon_{X1} = \varepsilon_{Z1}$. Similarly, the second resonance at 2.9 eV corresponds to a disk-shaped real part of the dielectric tensor with cylindrical symmetry, $\varepsilon_{Y1} < \varepsilon_{X1} = \varepsilon_{Z1}$. Due to the debatable assumptions involved in the relation between the electronic transport gap and the HOMO-LUMO peak-to-peak gap, we refrain from comparing this transport gap to specific signatures of the dielectric tensor like the energies where its real part has cylindrical symmetry or to absorptive excitonic features in its imaginary part. Finally, it is worth noting that the dipole-allowed higher lying transitions of intramolecular origin around 5 eV are resolved as a Davydov split doublet at 4.88 (Z)–4.94 (Y) eV located on the {102} crystal plane.

7. Conclusions

In this work we have obtained the dielectric tensor components of a monoclinic crystal, namely the α polymorph of 3,4,9,10-perylene tetracarboxylic dianhydride (α-PTCDA) in the 1.4 to 5.0 eV energy range. Data analysis taking into account the crystal symmetry directly connects the sample properties to standard ellipsometric angles tanΨ and cosΔ. From the measurements we derived the diagonalized tensor components ε_X, ε_Y, and ε_Z, where Y was chosen as the monoclinic axis.

Therefore, monoclinic behavior allowed rotation of the axes X and Z, in the plane perpendicular to the unique symmetry axis Y. This effect was the origin of the presence of three main structures in the weak ε_X component when a resonance effect with the stronger ε_Z component occurred. The three features were located at the energies 2.46 ± 0.02 eV, 2.95 ± 0.05 eV, and 3.9 ± 0.1 eV. These three observed electronic resonances are consistent with prominent critical points of the electronic joint density-of-states in the measured energy range, which seem related to the maximum optical absorption (sometimes identified as the optical gap), the HOMO-LUMO edge-to-edge transport gap, and the HOMO-LUMO peak-to-peak gap, although their assignments are more precisely discussed as due to several higher-lying CT intermolecular transitions.

CRediT authorship contribution statement

M.I. Alonso: Conceptualization, Methodology, Investigation, Visualization, Writing – original draft, Writing – review & editing. **M. Garriga:** Conceptualization, Methodology, Software, Visualization, Writing – review & editing. **J.O. Ossó:** Investigation. **F. Schreiber:** Interpretation, Writing – review & editing. **R. Scholz:** Methodology, Investigation, Writing – original draft, Writing – review & editing.

Declaration of competing interest

The authors declare that they have no known competing financial interests or personal relationships that could have appeared to influence the work reported in this paper.

Data availability

Data will be made available on request.

Acknowledgments

We dedicate this paper to the memory of Norbert Karl and Manuel Cardona who encouraged this work in its beginnings. MIA and MG acknowledge funding by the Spanish Ministerio de Ciencia e Innovación (MICINN) through grants PID2019-106860GB-I00 (highN) and CEX2019-000917-S (FUNFUTURE, in the framework of the Spanish Severo Ochoa Centre of Excellence program), as well as AGAUR, Spain for grant 2017-SGR-00488. FS and RS wish to acknowledge financial support from the DFG, Germany.

References

[1] G.E. Jellison, Data analysis for spectroscopic ellipsometry, in: H.G. Tompkins, E.A. Irene (Eds.), Handbook of Ellipsometry, William Andrew Publishing, Norwich, NY, 2005, pp. 237–296, http://dx.doi.org/10.1016/B978-081551499-2.50005-8.

[2] R.M.A. Azzam, N.M. Bashara, Ellipsometry and Polarized Light, North-Holland, Amsterdam, 1977.

[3] M. Born, E. Wolf, A.B. Bhatia, P.C. Clemmow, D. Gabor, A.R. Stokes, A.M. Taylor, P.A. Wayman, W.L. Wilcock, Principles of Optics: Electromagnetic Theory of Propagation, Interference and Diffraction of Light, seventh ed., Cambridge University Press, Cambridge, UK, 2002, http://dx.doi.org/10.1017/CBO9781139644181.

[4] D. Franta, Symmetry of linear dielectric response tensors: Dispersion models fulfilling three fundamental conditions, J. Appl. Phys. 127 (2020) 223101, http://dx.doi.org/10.1063/5.0005735.

[5] M.I. Alonso, M. Garriga, Optical properties of anisotropic materials: an experimental approach, Thin Solid Films 455–456 (2004) 124–131, http://dx.doi.org/10.1016/j.tsf.2003.12.061.

[6] D.E. Aspnes, Approximate solution of ellipsometric equations for optically biaxial crystals, J. Opt. Soc. Amer. 70 (10) (1980) 1275–1277, http://dx.doi.org/10.1364/JOSA.70.001275.

[7] D.E. Aspnes, Recent progress in the nondestructive analysis of surfaces, thin films, and interfaces by spectroellipsometry, Appl. Surf. Sci. 123 (1985) 792–803, http://dx.doi.org/10.1016/0378-5963(85)90212-0.

[8] L. Graf, F. Liu, M. Naumann, F. Roth, B. Debnath, B. Büchner, Y. Krupskaya, A.A. Popov, M. Knupfer, Optical anisotropy and momentum-dependent excitons in dibenzopentacene single crystals, ACS Omega 7 (2022) 21183–21191, http://dx.doi.org/10.1021/acsomega.2c01987.

[9] M. Dressel, B. Gompf, D. Faltermeier, A. Tripathi, J. Pflaum, M. Schubert, Kramers-Kronig-consistent optical functions of anisotropic crystals: generalized spectroscopic ellipsometry on pentacene, Opt. Express 16 (2008) 19770–19778, http://dx.doi.org/10.1364/OE.16.019770.

[10] C. Sturm, S. Höfer, K. Hingerl, T.G. Mayerhöfer, M. Grundmann, Dielectric function decomposition by dipole interaction distribution: application to triclinic $K_2Cr_2O_7$, New J. Phys. 22 (2020) 073041, http://dx.doi.org/10.1088/1367-2630/ab99df.

[11] O. Arteaga, Useful Mueller matrix symmetries for ellipsometry, Thin Solid Films 571 (2014) 584–588, http://dx.doi.org/10.1016/j.tsf.2013.10.101.

[12] W.D. Nesse, Introduction to Mineralogy, third ed., Oxford University Press, 2016.

[13] M. Möbus, N. Karl, T. Kobayashi, Structure of perylene-tetracarboxylic-dianhydride thin films on alkali halide crystal substrates, J. Cryst. Growth 116 (1992) 495–504, http://dx.doi.org/10.1016/0022-0248(92)90658-6.

[14] A.J. Lovinger, S.R. Forrest, M.L. Kaplan, P.H. Schmidt, T. Venkatesan, Structural and morphological investigation of the development of electrical conductivity in ion-irradiated thin films of an organic material, J. Appl. Phys. 55 (1984) 476–482, http://dx.doi.org/10.1063/1.333049.

[15] F. Schreiber, Organic molecular beam deposition: Growth studies beyond the first monolayer, Phys. Status Solidi (A) 201 (2004) 1037–1054, http://dx.doi.org/10.1002/pssa.200404334.

[16] G. Witte, C. Wöll, Growth of aromatic molecules on solid substrates for applications in organic electronics, J. Mater. Res. 19 (2004) 1889–1916, http://dx.doi.org/10.1557/JMR.2004.0251.

[17] P. Fenter, F. Schreiber, L. Zhou, P. Eisenberger, S.R. Forrest, In situ studies of morphology, strain, and growth modes of a molecular organic thin film, Phys. Rev. B 56 (1997) 3046–3053, http://dx.doi.org/10.1103/PhysRevB.56.3046.

[18] B. Krause, F. Schreiber, H. Dosch, A. Pimpinelli, O.H. Seeck, Temperature-dependence of the 2D-3D transition in the growth of PTCDA on Ag(111): a real-time x-ray and kinetic monte-carlo study, Europhys. Lett. 65 (2004) 372–378, http://dx.doi.org/10.1209/epl/i2003-10090-6.

[19] F. Tautz, Structure and bonding of large aromatic molecules on noble metal surfaces: The example of PTCDA, Prog. Surf. Sci. 82 (2007) 479–520, http://dx.doi.org/10.1016/j.progsurf.2007.09.001.

[20] A.A. Levin, T. Leisegang, R. Forker, M. Koch, D.C. Meyer, T. Fritz, Preparation and crystallographic characterization of crystalline modifications of 3, 4:9, 10-perylenetetracarboxylic dianhydride at room temperature, Cryst. Res. Technol. 45 (2010) 439–448, http://dx.doi.org/10.1002/crat.200900730.

[21] A. Hinderhofer, U. Heinemeyer, A. Gerlach, S. Kowarik, R.M.J. Jacobs, Y. Sakamoto, T. Suzuki, F. Schreiber, Optical properties of pentacene and perfluoropentacene thin films, J. Chem. Phys. 127 (2007) 194705, http://dx.doi.org/10.1063/1.2786992.

[22] U. Heinemeyer, K. Broch, A. Hinderhofer, M. Kytka, R. Scholz, A. Gerlach, F. Schreiber, Real-time changes in the optical spectrum of organic semiconducting films and their thickness regimes during growth, Phys. Rev. Lett. 104 (2010) 257401, http://dx.doi.org/10.1103/PhysRevLett.104.257401.

[23] D. Bellinger, J. Pflaum, C. Brüning, V. Engel, B. Engels, The electronic character of PTCDA thin films in comparison to other perylene-based organic semiconductors: ab initio-, TD-DFT and semi-empirical computations of the opto-electronic properties of large aggregates, Phys. Chem. Chem. Phys. 19 (2017) 2434–2448, http://dx.doi.org/10.1039/C6CP07673D.

[24] M.I. Alonso, M. Garriga, N. Karl, J.O. Ossó, F. Schreiber, Anisotropic optical properties of single crystalline PTCDA studied by spectroscopic ellipsometry, Org. Electron. 3 (2002) 23–31, http://dx.doi.org/10.1016/S1566-1199(01)00027-1.

[25] W. Lang, R. Claus, Geometrical dispersion of dielectric and optic axes in a monoclinic crystal, Phys. Rev. B 26 (1982) 7119–7122, http://dx.doi.org/10.1103/PhysRevB.26.7119.

[26] A.B. Kuzmenko, E.A. Tishchenko, V.G. Orlov, Transverse optic modes in monoclinic α-Bi_2O_3, J. Phys.: Condens. Matter 8 (1996) 6199–6212, http://dx.doi.org/10.1088/0953-8984/8/34/010.

[27] C. Sturm, J. Furthmüller, F. Bechstedt, R. Schmidt-Grund, M. Grundmann, Dielectric tensor of monoclinic Ga_2O_3 single crystals in the spectral range 0.5–8.5 eV, APL Mater. 3 (10) (2015) 106106, http://dx.doi.org/10.1063/1.4934705.

[28] G.E. Jellison Jr., M.A. McGuire, L.A. Boatner, J.D. Budai, E.D. Specht, D.J. Singh, Spectroscopic dielectric tensor of monoclinic crystals: $CdWO_4$, Phys. Rev. B 84 (2011) 195439, http://dx.doi.org/10.1103/PhysRevB.84.195439.

[29] J. Gerald, E. Jellison, E.D. Specht, L.A. Boatner, D.J. Singh, C.L. Melcher, Spectroscopic refractive indices of monoclinic single crystal and ceramic lutetium oxyorthosilicate from 200 to 850 nm, J. Appl. Phys. 112 (2012) 063524, http://dx.doi.org/10.1063/1.4752421.

[30] R. Scholz, A.Y. Kobitski, D.R.T. Zahn, M. Schreiber, Investigation of molecular dimers in α-PTCDA by ab initio methods: Binding energies, gas-to-crystal shift, and self-trapped excitons, Phys. Rev. B 72 (2005) 245208, http://dx.doi.org/10.1103/PhysRevB.72.245208.

[31] M. Wewer, F. Stienkemeier, Laser-induced fluorescence spectroscopy of 3, 4, 9, 10-perylenetetracarboxylic-dianhydride in helium nanodroplets, J. Chem. Phys. 120 (2004) 1239–1244, http://dx.doi.org/10.1063/1.1633761.

[32] V. Bulović, P. Burrows, S. Forrest, J. Cronin, M. Thompson, Study of localized and extended excitons in 3, 4, 9, 10-perylenetetracarboxylic dianhydride (PTCDA) i. spectroscopic properties of thin films and solutions, Chem. Phys. 210 (1996) 1–12, http://dx.doi.org/10.1016/0301-0104(96)00114-0, confined Excitations in Molecular and Semiconductor Nanostructures.

[33] E. Engel, K. Schmidt, D. Beljonne, J.-L. Brédas, J. Assa, H. Fröb, K. Leo, M. Hoffmann, Transient absorption spectroscopy and quantum-chemical studies of matrix-isolated perylene derivatives, Phys. Rev. B 73 (2006) 245216, http://dx.doi.org/10.1103/PhysRevB.73.245216.

[34] R. Scholz, A. Kobitski, T. Kampen, M. Schreiber, D. Zahn, G. Jungnickel, M. Elstner, M. Sternberg, T. Frauenheim, Resonant Raman spectroscopy of 3, 4, 9, 10-perylene-tetracarboxylic-dianhydride epitaxial films, Phys. Rev. B 61 (2000) 13659–13669, http://dx.doi.org/10.1103/PhysRevB.61.13659.

[35] M. Friedrich, T. Wagner, G. Salvan, S. Park, T. Kampen, D. Zahn, Optical constants of 3, 4, 9, 10-perylenetetracarboxylic dianhydride films on silicon and gallium arsenide studied by spectroscopic ellipsometry, Appl. Phys. A 75 (2002) 501–506, http://dx.doi.org/10.1007/s003390101001.

[36] K. Gustav, M. Leonhardt, H. Port, Theoretical investigations on absorption and fluorescence of perylene and its tetracarboxylic derivatives, Monatsh. Chem. 128 (1997) 105–112, http://dx.doi.org/10.1007/BF00807299.

[37] M. Tahir, Muddusir, D.N. Khan, S. Gul, F. Wahab, S.M. Said, Photovoltaic effect on the microelectronic properties of perylene/p-Si heterojunction devices, J. Mater. Sci.: Mater. Electron. 30 (2019) 19463–19470, http://dx.doi.org/10.1007/s10854-019-02310-z.

[38] E.V. Tsiper, Z.G. Soos, Charge redistribution and polarization energy of organic molecular crystals, Phys. Rev. B 64 (2001) 195124, http://dx.doi.org/10.1103/PhysRevB.64.195124.

[39] I. Hill, A. Kahn, Z. Soos, R. Pascal Jr., Charge-separation energy in films of π-conjugated organic molecules, Chem. Phys. Lett. 327 (2000) 181–188, http://dx.doi.org/10.1016/S0009-2614(00)00882-4.

[40] S. Krause, M.B. Casu, A. Schöll, E. Umbach, Determination of transport levels of organic semiconductors by UPS and IPS, New J. Phys. 10 (2008) 085001, http://dx.doi.org/10.1088/1367-2630/10/8/085001.

[41] M. Anderson, V. Williams, T. Schuerlein, G. Collins, C. England, L.-K. Chau, P. Lee, K. Nebesny, N. Armstrong, RHEED and optical characterization of ordered multilayers of phthalocyanine/C_{60} and phthalocyanine/perylene-tetracarboxylicdianhydride (PTCDA), Surf. Sci. 307–309 (1994) 551–558, http://dx.doi.org/10.1016/0039-6028(94)90452-9.

[42] H. Proehl, T. Dienel, R. Nitsche, T. Fritz, Formation of solid-state excitons in ultrathin crystalline films of PTCDA: From single molecules to molecular stacks, Phys. Rev. Lett. 93 (2004) 097403, http://dx.doi.org/10.1103/PhysRevLett.93.097403.

[43] R. Scholz, I. Vragović, A.Y. Kobitski, G. Salvan, T.U. Kampen, M. Schreiber, D.R.T. Zahn, Spectroscopic properties of a prototypic organic semiconductor: The case of PTCDA, in: Proceedings of the International School of Physics Enrico Fermi, Vol. 149, 2002, pp. 379–403, http://dx.doi.org/10.3254/978-1-61499-005-5-379.

[44] I. Vragović, R. Scholz, J. Šetrajčić, Optical properties of PTCDA bulk crystals and ultrathin films, in: Recent Developments in Advanced Materials and Processes, in: Materials Science Forum, vol. 518, Trans Tech Publications Ltd, 2006, pp. 41–46, http://dx.doi.org/10.4028/www.scientific.net/MSF.518.41.

[45] L. Gisslén, R. Scholz, Crystallochromy of perylene pigments: Interference between Frenkel excitons and charge-transfer states, Phys. Rev. B 80 (2009) 115309, http://dx.doi.org/10.1103/PhysRevB.80.115309.

[46] V.R. Gangilenka, L.V. Titova, L.M. Smith, H.P. Wagner, L.A.A. DeSilva, L. Gisslén, R. Scholz, Selective excitation of exciton transitions in PTCDA crystals and films, Phys. Rev. B 81 (2010) 155208, http://dx.doi.org/10.1103/PhysRevB.81.155208.

[47] A.Y. Kobitski, R. Scholz, I. Vragović, H. Wagner, D. Zahn, Low-temperature time-resolved photoluminescence characterization of 3, 4, 9, 10-perylene tetracarboxylic dianhydride crystals, Phys. Rev. B 66 (2002) 153204, http://dx.doi.org/10.1103/PhysRevB.66.153204.

[48] A.Y. Kobitski, R. Scholz, D.R.T. Zahn, H.P. Wagner, Time-resolved photoluminescence study of excitons in α-PTCDA as a function of temperature, Phys. Rev. B 68 (2003) 155201, http://dx.doi.org/10.1103/PhysRevB.68.155201.

[49] T. Ogawa, K. Kuwamoto, S. Isoda, T. Kobayashi, N. Karl, 3, 4:9, 10-perylenetetracarboxylic dianhydride (PTCDA) by electron crystallography, Acta Cryst. B55 (1999) 123–130, http://dx.doi.org/10.1107/s0108768198009872.

[50] J.F. Nye, Physical Properties of Crystals, 1985th ed., Oxford University Press, Oxford, UK, 2000.

[51] D.W. Berreman, Optics in smoothly varying anisotropic planar structures - application to liquid-crystal twist cells, J. Opt. Soc. Amer. 63 (11) (1973) 1374–1380, http://dx.doi.org/10.1364/JOSA.63.001374.

[52] M.I. Alonso, M. Garriga, J.O. Ossó, F. Schreiber, R. Scholz, The dielectric tensor of monoclinic α-3, 4, 9, 10-perylene tetracarboxylic dianhydride in the visible spectral range, Thin Solid Films 571 (2014) 420–425, http://dx.doi.org/10.1016/j.tsf.2013.11.034.

[53] D.W. Berreman, Optics in stratified and anisotropic media: 4 × 4 matrix formulation, J. Opt. Soc. Amer. 62 (4) (1972) 502–510, http://dx.doi.org/10.1364/JOSA.62.000502.

[54] P. Yeh, Optics of anisotropic layered media: A new 4 × 4 matrix algebra, Surf. Sci. 96 (1) (1980) 41–53, http://dx.doi.org/10.1016/0039-6028(80)90293-9.

[55] D.E. Aspnes, The accurate determination of optical properties by ellipsometry, in: E.D. Palik (Ed.), Handbook of Optical Constants of Solids, Vol. 1, Academic Press, New York, 1985, pp. 89–112, Ch. 5.

[56] E.I. Haskal, Z. Shen, P.E. Burrows, S.R. Forrest, Excitons and exciton confinement in crystalline organic thin films grown by organic molecular-beam deposition, Phys. Rev. B 51 (1995) 4449–4462, http://dx.doi.org/10.1103/PhysRevB.51.4449.

[57] U. Hörmann, J. Kraus, M. Gruber, C. Schuhmair, T. Linderl, S. Grob, S. Kapfinger, K. Klein, M. Stutzman, H.J. Krenner, W. Brütting, Quantification of energy losses in organic solar cells from temperature-dependent device characteristics, Phys. Rev. B 88 (2013) 235307, http://dx.doi.org/10.1103/PhysRevB.88.235307.

[58] J. Widmer, M. Tietze, K. Leo, M. Riede, Open-circuit voltage and effective gap of organic solar cells, Adv. Funct. Mater. 23 (2013) 5814–5821, http://dx.doi.org/10.1002/adfm.201301048.

[59] K. Vandewal, K. Tvingstedt, A. Gadisa, O. Inganäs, J.V. Manca, Relating the open-circuit voltage to interface molecular properties of donor:acceptor bulk heterojunction solar cells, Phys. Rev. B 81 (2010) 125204, http://dx.doi.org/10.1103/PhysRevB.81.125204.

[60] M. Gruber, J. Wagner, K. Klein, U. Hörmann, A. Opitz, M. Stutzmann, W. Brütting, Thermodynamic efficiency limit of molecular donor–acceptor solar cells and its application to diindenoperylene/ C_{60}-based planar heterojunction devices, Adv. Energy Mater. 2 (2012) 1100–1108, http://dx.doi.org/10.1002/aenm.201200077.

[61] M.L. Tietze, W. Tress, S. Pfützner, C. Schünemann, L. Burtone, M. Riede, K. Leo, K. Vandewal, S. Olthof, P. Schulz, A. Kahn, Correlation of open-circuit voltage and energy levels in zinc-phthalocyanine: C_{60} bulk heterojunction solar cells with varied mixing ratio, Phys. Rev. B 88 (2013) 085119, http://dx.doi.org/10.1103/PhysRevB.88.085119.

[62] D. Beljonne, H. Yamagata, J.L. Brédas, F.C. Spano, Y. Olivier, Charge-transfer excitations steer the Davydov splitting and mediate singlet exciton fission in pentacene, Phys. Rev. Lett. 110 (2013) 226402, http://dx.doi.org/10.1103/PhysRevLett.110.226402.

[63] K. Broch, J. Dieterle, F. Branchi, N.J. Hestand, Y. Olivier, H. Tamura, C. Cruz, V.M. Nichols, A. Hinderhofer, D. Beljonne, F.C. Spano, G. Cerullo, C.J. Bardeen, F. Schreiber, Robust singlet fission in pentacene thin films with tuned charge transfer interactions, Nature Commun. 9 (2018) 954, http://dx.doi.org/10.1038/s41467-018-03300-1.

[64] R. Scholz, R. Luschtinetz, G. Seifert, T. Jägeler-Hoheisel, C. Körner, K. Leo, M. Rapacioli, Quantifying charge transfer energies at donor–acceptor interfaces in small-molecule solar cells with constrained DFTB and spectroscopic methods, J. Phys.: Condens. Matter 25 (2013) 473201, http://dx.doi.org/10.1088/0953-8984/25/47/473201.

[65] K. Vandewal, J. Benduhn, K.S. Schellhammer, T. Vangerven, J.E. Rückert, F. Piersimoni, R. Scholz, O. Zeika, Y. Fan, S. Barlow, D. Neher, S.R. Marder, J. Manca, D. Spoltore, G. Cuniberti, F. Ortmann, Absorption tails of donor:C_{60} blends provide insight into thermally activated charge-transfer processes and polaron relaxation, J. Am. Chem. Soc. 139 (2017) 1699–1704, http://dx.doi.org/10.1021/jacs.6b12857.

[66] D.R. Zahn, G.N. Gavrila, M. Gorgoi, The transport gap of organic semiconductors studied using the combination of direct and inverse photoemission, Chem. Phys. 325 (2006) 99–112, http://dx.doi.org/10.1016/j.chemphys.2006.02.003.